The Astrophysical Journal, 775:24 (16pp), 2013 September 20 doi:10.1088/0004-637X/775/1/24

HELIOSPHERIC ENERGETIC NEUTRAL HYDROGEN MEASURED WITH ASPERA-3 AND ASPERA-4

A. Galli[1], P. Wurz[1], P. Kollmann[2], P. C. Brandt[2], M. Bzowski[3], J. M. Sokół[3], M. A. Kubiak[3], A. Grigoriev[4], and S. Barabash[5]
[1] Physics Institute, University of Bern, Bern 3012, Switzerland
[2] The Johns Hopkins University, Applied Physics Laboratory, Laurel, MD 20723, USA
[3] Space Research Centre, Polish Academy of Sciences, Warsaw 00-716, Poland
[4] Space Research Institute (IKI), Moscow 117997, Russia
[5] The Swedish Institute of Space Physics, Kiruna SE-981 28, Sweden
Received 2013 March 22; accepted 2013 July 25; published 2013 August 30

ABSTRACT

We re-analyze the signal of non-planetary energetic neutral atoms (ENAs) in the 0.4–5.0 keV range measured with the Neutral Particle Detector (NPD) of the ASPERA-3 and ASPERA-4 experiments on board the *Mars* and *Venus Express* satellites. Due to improved knowledge of sensor characteristics and exclusion of data sets affected by instrument effects, the typical intensity of the ENA signal obtained by ASPERA-3 is an order of magnitude lower than in earlier reports. The ENA intensities measured with ASPERA-3 and ASPERA-4 now agree with each other. In the present analysis, we also correct the ENA signal for Compton–Getting and for ionization loss processes under the assumption of a heliospheric origin. We find spectral shapes and intensities consistent with those measured by the *Interstellar Boundary Explorer* (*IBEX*). The principal advantage of ASPERA with respect to the *IBEX* sensors is the two times better spectral resolution. In this study, we discuss the physical significance of the spectral shapes and their potential variation across the sky. At present, these observations are the only independent test of the heliospheric ENA signal measured with *IBEX* in this energy range. The ASPERA measurements also allow us to check for a temporal variation of the heliospheric signal as they were obtained between 2003 and 2007, whereas *IBEX* has been operational since the end of 2008.

Key words: ISM: general – plasmas – solar wind – Sun: heliosphere

Online-only material: color figures

1. INTRODUCTION

1.1. Imaging of ENAs from the Heliosphere

The heliosphere is created by the solar wind that rams into the surrounding local interstellar medium. The interaction region between solar wind and surrounding plasma comprises two distinct boundaries. At the termination shock, the solar wind is abruptly slowed down from supersonic to subsonic speed. Further away from the Sun, the heliopause separates solar wind plasma from interstellar plasma. The termination shock has been identified by the *Voyager* spacecraft to be between 80 and 100 AU away from the Sun (Burlaga et al. 2008; Richardson et al. 2008).

Heliospheric energetic neutral atoms (ENAs) predominantly originate from the heliosheath between the termination shock and the heliopause. There, hydrogen ENAs are produced by charge exchange between interstellar neutral atoms and protons from the solar wind, from pickup ions, or from other ion populations (Chalov et al. 2003). These processes are predicted to result in a flux of inward moving ENAs detectable at Earth orbit (Gruntman et al. 2001). Imaging these ENAs provides information on the termination shock, the heliosheath surrounding it, and in general about the interaction of the solar wind with the local interstellar medium.

1.2. Context of This Study

The first results on non-planetary ENAs measured with NPD/ASPERA-3 on *Mars Express* (*MEX*) were published by Galli et al. (2006a) and Wurz et al. (2008). The signal was considered non-planetary because it was already measured during cruise phase, far away from Mars, and was generally unrelated to the interaction of the solar wind with the Martian magnetosphere. The authors reported a typical intensity of the ENA signal of 10^4 cm^{-2} sr^{-1} s^{-1} between 0.3 and 10 keV. Based on measurements with NPD/ASPERA-4 on *Venus Express* (*VEX*), Brandt et al. (2009) reported ENA intensities of only 10^2–10^3 cm^{-2} sr^{-1} s^{-1}. The *Interstellar Boundary Explorer* (*IBEX*; McComas et al. 2009a), in operation since the end of 2008, was specifically designed to image ENAs from the heliospheric interaction region (Wieser et al. 2007). *IBEX* is recording spatially and spectrally resolved ENA images at a higher instrument sensitivity than ASPERA. The ENA intensities measured with *IBEX* (e.g., McComas et al. 2009b) were of the same order of magnitude as derived from ASPERA-4 measurements (Brandt et al. 2009) and roughly one order of magnitude lower than those reported from the first NPD/ASPERA-3 measurements. A more precise comparison between ASPERA and *IBEX* results was impossible, because none of the mentioned ASPERA publications included correction for re-ionization losses in the heliosphere. Moreover, Galli et al. (2006a) neglected the motion of the spacecraft relative to the ENAs, whereas Brandt et al. (2009) neglected the time-dependent sensor degradation.

The present work investigates whether the discrepancy between NPD/ASPERA-3 and NPD/ASPERA-4 still exists and if the signal measured with ASPERA, after compensating for ionization losses, is consistent with the *IBEX* results. For this goal, we re-assessed all NPD/ASPERA-3 and NPD/ASPERA-4 measurements suitable for the observation of heliospheric ENAs. The data sets are limited because the Neutral Particle Detector (NPD) sensors were primarily operated to study the interaction of the solar wind with the planetary atmospheres of Mars (ASPERA-3) and Venus (ASPERA-4) (Galli et al. 2008a,

2008b). In terms of observation time, spatial resolution, and sensitivity, the *IBEX* sensors are much better suited to observe heliospheric ENAs. The only advantage of the NPD/ASPERA sensors is the higher energy resolution; the FWHM of the instrument response corresponds to $\Delta E/E = 0.45$ compared to 0.8 of the *IBEX*-Lo sensor (Fuselier et al. 2009) and to 0.6 of the *IBEX*-Hi sensor (Funsten et al. 2009).

The present study improves on the previous work done by Galli et al. (2006a), Wurz et al. (2008), and Brandt et al. (2009) in many respects. First, all available measurements of ASPERA-3 and ASPERA-4 were included. This allows for a further consistency check for varying heliocentric distance of observer position. The ENA signals were re-evaluated based on the final NPD instrument calibration (Grigoriev 2007) and the time-dependent detection efficiencies of NPD/ASPERA-4 were compensated for. The Compton–Getting effect due to the spacecraft motion was also taken into account. Finally, the intensities were corrected for the survival probabilities of ENAs along their travel from the heliospheric boundary to the location of detection (see Bzowski et al. 2013 and Appendix 2 in McComas et al. 2012).

1.3. Structure of the Paper

In Section 2 we characterize the NPD instruments, the data selection criteria, and we explain how the measured count rates were converted into ENA intensities. Section 3 summarizes the results. In Section 4 we discuss if the ASPERA results are consistent with other observations of heliospheric ENAs, in particular with the most recent *IBEX* results (McComas et al. 2012; Fuselier et al. 2012). Section 5 concludes the paper.

2. INSTRUMENTATION AND OBSERVATIONS

The ASPERA-3 and ASPERA-4 experiments are copies of each other, designed to measure ions, electrons, and ENAs on board the ESA missions *MEX* and *VEX* (Barabash et al. 2006, 2007). *MEX* was launched in 2003, entering Mars orbit in 2003 December; *VEX* was launched in 2005, entering Venus orbit in 2006 April.

2.1. NPD Observations with ASPERA-3/MEX and ASPERA-4/VEX

NPD is a pin-hole camera designed to measure hydrogen and oxygen ENAs at energies between 0.3 and 10 keV, using the time-of-flight (TOF) technique. The instrument consists of two identical sensors, NPD1 and NPD2. Each sensor has one start and three stop surfaces that provide an angular resolution of roughly 40° in azimuthal direction and 6° in elevation direction, giving a total instantaneous field of view (FOV) of 180° × 6° (Grigoriev 2007). The pure (energy-independent) geometric factor is 0.01 cm^2 sr per stop surface, the absolute efficiency of the sensor lies between 0.1% and 10% depending on the energy of the ENA.

The upper panel of Figure 1 shows an engineering drawing of NPD, the black arrows indicate the viewing directions defined by the three stop surfaces. Incoming ENA particles at the upper left pass between two parallel deflector plates, separated by a gap with an interplate electric potential difference of up to 10 kV, and enter a pin-hole of 3.0 × 4.5 mm^2 size. Charged particles with an energy of less than 70 keV per charge are swept away by the transverse electric field created between the plates. ENAs entering the camera first trigger a signal from the start surface

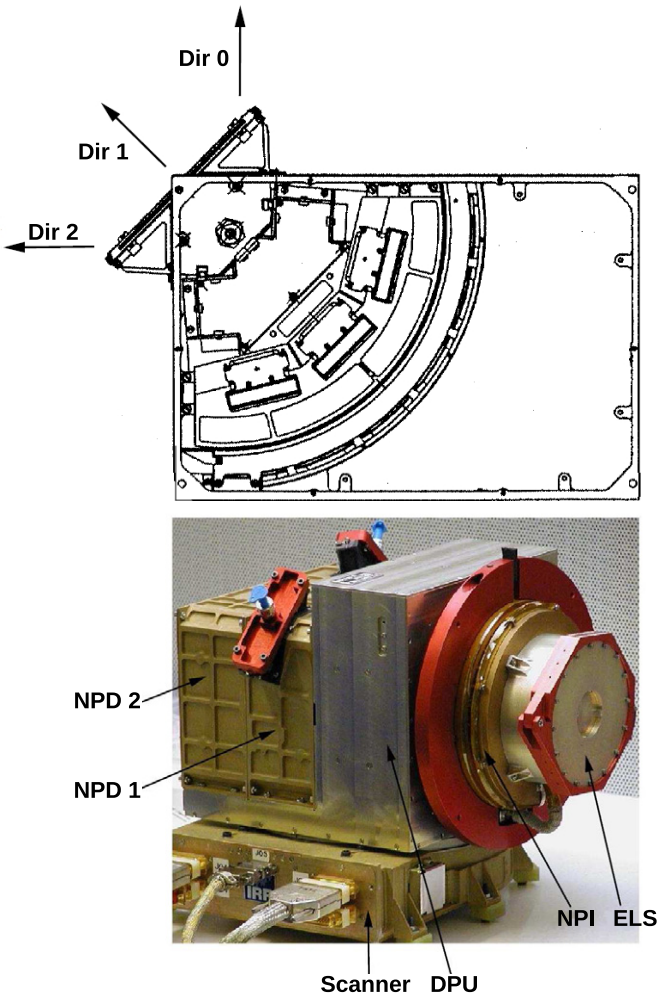

Figure 1. Neutral Particle Detector as a part of the ASPERA-3 experiment. Upper panel: engineering drawing of one of the NPD sensors; black arrows indicate the three directions defined by the three stop micro-channel plates. Lower panel: photograph of the entire main unit of ASPERA-3 before it was mounted on *MEX*. Images taken from Grigoriev (2007).

(A color version of this figure is available in the online journal.)

and then, after an 8 cm path length, hit the stop surface (the continuous black quadrant in Figure 1). The secondary electrons triggered by the impact are registered by one of the three stop micro-channel plates. This signal also defines the incoming direction 0, 1, or 2 of the ENA. The energy and the mass of the particle can be reconstructed from the TOF between the start and the stop surface and from the pulse height of the stop signal. Principally, this design enables NPD to distinguish oxygen from hydrogen ENAs. Only those events with one correlated start and stop signal will be used for analysis.

The lower panel in Figure 1 shows the complete main unit of the ASPERA-3 experiment with NPD1 and NPD2, the Digital Processing Unit, the Neutral Particle Imager, and the Electron Spectrometer. The whole experiment is mounted on a scanning platform, which itself is rigidly mounted on the spacecraft. This means that the two directions 0 of NPD1 and NPD2 point away from the spacecraft, whereas the directions 2 point away from each other and almost parallel to the spacecraft surface.

Figure 2 shows an example of a non-planetary ENA signal, measured on 2006 June 7. The top panel shows the FOVs in the ecliptic reference frame, the black cross denotes the Sun direction, red asterisks outline the limb of the solar panel, and the red oval is the Venus limb. The middle panel shows the

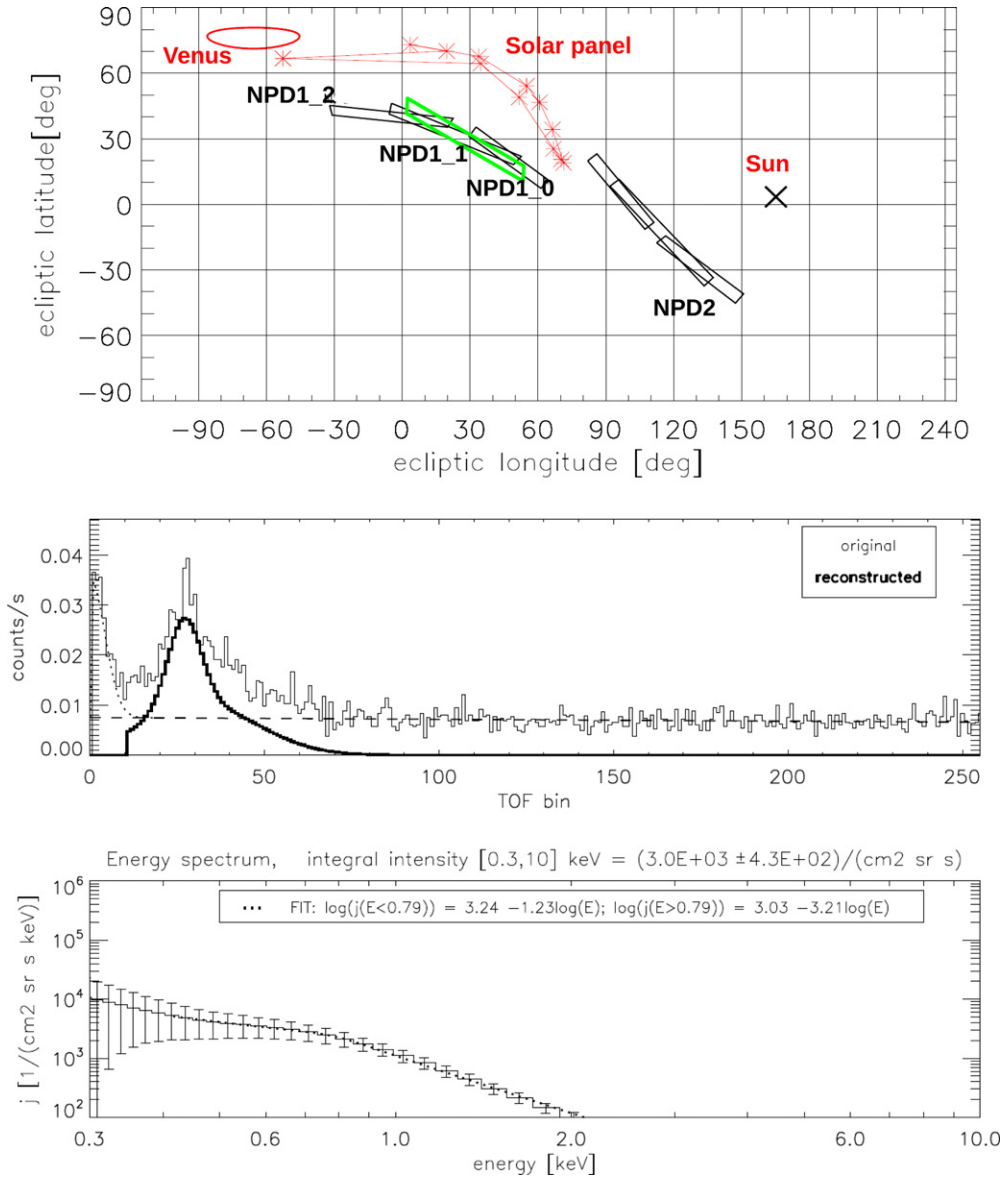

Figure 2. Non-planetary ENA signal measured in the sector NPD1_1 of ASPERA-4 on 2006 June 7 (marked green in the top panel), accumulated over 45 minutes. Top panel: pointing direction of FOVs, middle panel: raw TOF spectrum (thin line) and reconstructed TOF signal after noise subtraction and deconvolution (thick line). UV background denoted by dashed line. Bottom panel: differential ENA intensity from reconstructed TOF signal.

(A color version of this figure is available in the online journal.)

TOF signal, and the bottom panel shows the corresponding differential ENA intensity j: a power law with a knee at 0.79 keV, a high-energy slope of −3.21, and a low-energy slope of −1.23 (for conversion of TOF signal into ENA intensity, see Section 2.3). The 256 TOF bins shown in the middle panel of Figure 2 range from 0 to 2048 ns and define the velocity of the registered particle. This velocity is converted into energy based on the assumption that all measured non-planetary ENAs are hydrogen ENAs. Oxygen atoms at energies between 0.3 keV and 10 keV would produce a peak at a considerably longer TOF than the observed 200–400 ns. Electric deflection fields at the entrance slit sweep away all charged particles below 70 keV. UV photons, on the other hand, can enter the sensor and also contribute to the signal (indicated by the dashed line in the middle panel of Figure 2). They produce a flat background that is well understood (Galli et al. 2006b).

Other possible background sources (Wurz et al. 2009) are instrument electronics, penetrating radiation from cosmic rays (Reisenfeld et al. 2012), and spacecraft outgassing. The peak in the first six bins of the TOF spectrum seen in Figure 2 was likely caused by electronics. Galli et al. (2006a) showed by simulations that protons with energies larger than 100 keV, which cannot be deflected from the start surface, also would produce an exponentially decreasing peak in the first five TOF bins. For real measurements, however, the TOF peak hardly correlated with sky direction or spacecraft position, but it strongly depended on the NPD sector. This led us to conclude that it was an instrument-related feature rather than an external signal. For all NPD sectors considered in this publication, the peak occurred at TOF bins different from those of true hydrogen ENAs. It could therefore be fitted and subtracted before analysis. Count rates from penetrating radiation are unlikely to contribute to the TOF signal after the flat background has been subtracted. High-energy particles should have no preference to trigger start and stop events at time intervals mimicking 1 keV hydrogen atoms. To exclude spacecraft outgassing, we also verified that the TOF

signal remained constant over several hours of measurements (see subsequent section).

2.2. Data Selection

Given the weak intensity of heliospheric ENAs, it was crucial to exclude ENAs originating from Mars, Venus, or from local sources. Unfortunately, there were very few NPD observations from the cruise phase of *MEX* and *VEX*. Once the spacecraft had reached their destination, NPD was pointed toward the planet for most of the observation time. On each orbit, the spacecraft also passed through the various plasma boundaries around the planet, which could cause spurious signals. For the present analysis, we excluded all observations that matched any of the following criteria:

1. FOV closer than 30° to planetary limb.
2. Spacecraft inside planetary bow shock.
3. Observations after 2007 (degradation of NPD/ASPERA-4 due to UV light).
4. FOV obstructed by solar panel or closer than 97° to Sun direction.
5. Rapidly decreasing ENA intensity due to sensor or spacecraft outgassing.

The 30° cutoff to avoid planetary ENAs was derived from the observed ENA outflow at Venus (Galli et al. 2008a). The signals used in this study do not correlate with angular or radial distance to Venus or Mars. The position of the bow shock around Venus was estimated from the average observed during the first years of ASPERA-4 operations (Martinecz et al. 2008). The effect of UV degradation will be described in Section 2.3. The two last exclusion criteria warrant a more thorough explanation here.

Ions and electrons up to an energy of 70 keV are prevented from entering the NPD sensor by the deflection voltage. However, solar wind neutralized on metal surfaces of the spacecraft can enter the NPD sensor, mimicking a valid ENA signal. At a distance of 0.7 AU to the Sun, these signals can reach an intensity of 10^6 cm^{-2} sr^{-1} s^{-1} when the NPD FOV is directed at the illuminated edge of the solar panel (see lower panel in Figure 4). If we assume that these ENAs scatter isotropically to the hemisphere above the metal surface and estimate the solar wind flux at Venus to 4×10^8 cm^{-2} s^{-1} (Marsch et al. 1982), this implies that 1%–10% of the solar wind ions are neutralized and then reflected at the metal surface.

A signal of neutralized solar wind was also observed when the FOV was directed to the Sunward hemisphere but was not obstructed otherwise. Such an observation is shown in Figure 3. The derived energy spectrum from this measurement (bottom panel of Figure 3) is representative for all occurrences of solar wind contamination: a flat low-energy slope (-1.5 ± 0.4) gives way to a very steep slope at higher energies (-4.7 ± 0.5). The knee at 1.0 ± 0.2 keV corresponds to typical solar wind energies.

In Figure 4, we organized all apparent ENA intensities measured with NPD1/ASPERA-4 in 2006 according to the angular distance to the Sun (angle ξ_1) and the minimum angular distance to the solar panels (ξ_2). These angles are illustrated in the top panel of Figure 4. The angle ξ_1 is defined for *MEX* and *VEX* in the same way, ξ_2 is only needed for ASPERA-4 data analysis, because NPD/ASPERA-3 was not mounted on the same spacecraft side as the solar panels (Barabash et al. 2006). For the Sun angle plot (ξ_1, middle panel), only signals measured in NPD1_2 are shown for which ξ_2 was at least 7. Vice versa, for the plot of ξ_2 (angle to solar panel) only measurements were included for which ξ_1 was at least 97°. In the middle panel, the ENA intensities increase by two orders of magnitude when ξ_1 becomes smaller than 90°. Obviously, a part of the unperturbed solar wind (coming from Sun direction) was neutralized at the entrance slit of the sensor when the latter was not completely shadowed by the instrument or the spacecraft. Therefore, we excluded all NPD measurements from analysis if the angle to the Sun was less than 97° (red dashed line in middle panel). This cutoff angle can also be motivated theoretically. Assuming that the signal is caused by neutralized solar wind, the angular distance to the solar wind has to be at least 90° plus the thermal scatter angle of solar wind protons. According to Marsch et al. (1982), the scattering angle α around the bulk solar wind flow,

$$\alpha \approx \arctan \sqrt{\frac{k_B T}{E}}, \quad (1)$$

is 5°–6°.5 for any solar wind velocity between 300 and 700 km s^{-1}, with E being the proton energy and T being the kinetic temperature. The cutoff for the angular distance to the solar panel cannot be motivated by theory, and data with ξ_2 between 5° and 10° are virtually absent. The bottom panel of Figure 4 just shows that ENA intensities as large as 10^6 cm^{-2} sr^{-1} s^{-1} are to be expected once the FOV intersects the solar panel. We therefore set the cutoff to $\xi_2 = 7°$ (red dashed line in Figure 4) and verified in Section 3 that the results do not change if more stringent cutoffs $\xi_1 > 115°$ and $\xi_2 > 15°$ are applied.

These cutoffs are valid for unperturbed solar wind conditions. Inside the planetary bow shock, the ions exhibit a much larger scatter around the bulk flow direction. As a result, most observations made inside the bow shock are contaminated by ions neutralized on the spacecraft that dominate over the weak non-planetary signal.

The first work by Galli et al. (2006a) on non-planetary ENAs relied mostly on the NPD2/ASPERA-3 measurements obtained during the cruise phase of *MEX* to Mars (2003 July to 2004 January). Re-analysis of those data showed that in most cases the intensity decreased by a factor of two or more over 1 hr of observation time. During the first months of operation, this process repeated itself when the instrument was switched on again. The viewing direction and the spacecraft attitude did not change during these observation and none of the above-mentioned exclusion criteria applied. This fast decrease of intensity with time did not occur during later phases of the mission. Therefore, sensor outgassing is the most plausible explanation (Schläppi et al. 2010). NPD/ASPERA-4 on *VEX* never registered similar intensity decreases during a single observation. One reason might be that there were very few cruise phase observations. The temporal variability (for steps of 10 minutes) of the intensity was typically 10%–20%, which is similar to the error bars assigned to the average intensity. The potentially most useful NPD/ASPERA-3 observations of non-planetary ENAs were made in 2003 July, the very first month of ASPERA-3 observations, and showed clear signs of outgassing. For re-analysis, we thus faced the dilemma of either compensating for outgassing or discarding most of the NPD/ASPERA-3 data. The intensity decrease could not be described by a simple model, and different sectors and different days of observation showed a different decrease with time. Therefore, we decided to omit all ENA signals measured with NPD/ASPERA-3 for which the apparent intensity decreased by a factor of two or more after the instrument was switched on. All data ruled out by this criterion also showed much higher integral intensities of 10^4 cm^{-2} sr^{-1} s^{-1} at the begin of an observation period than later observations made with ASPERA-3 or ASPERA-4 (see Figure 5).

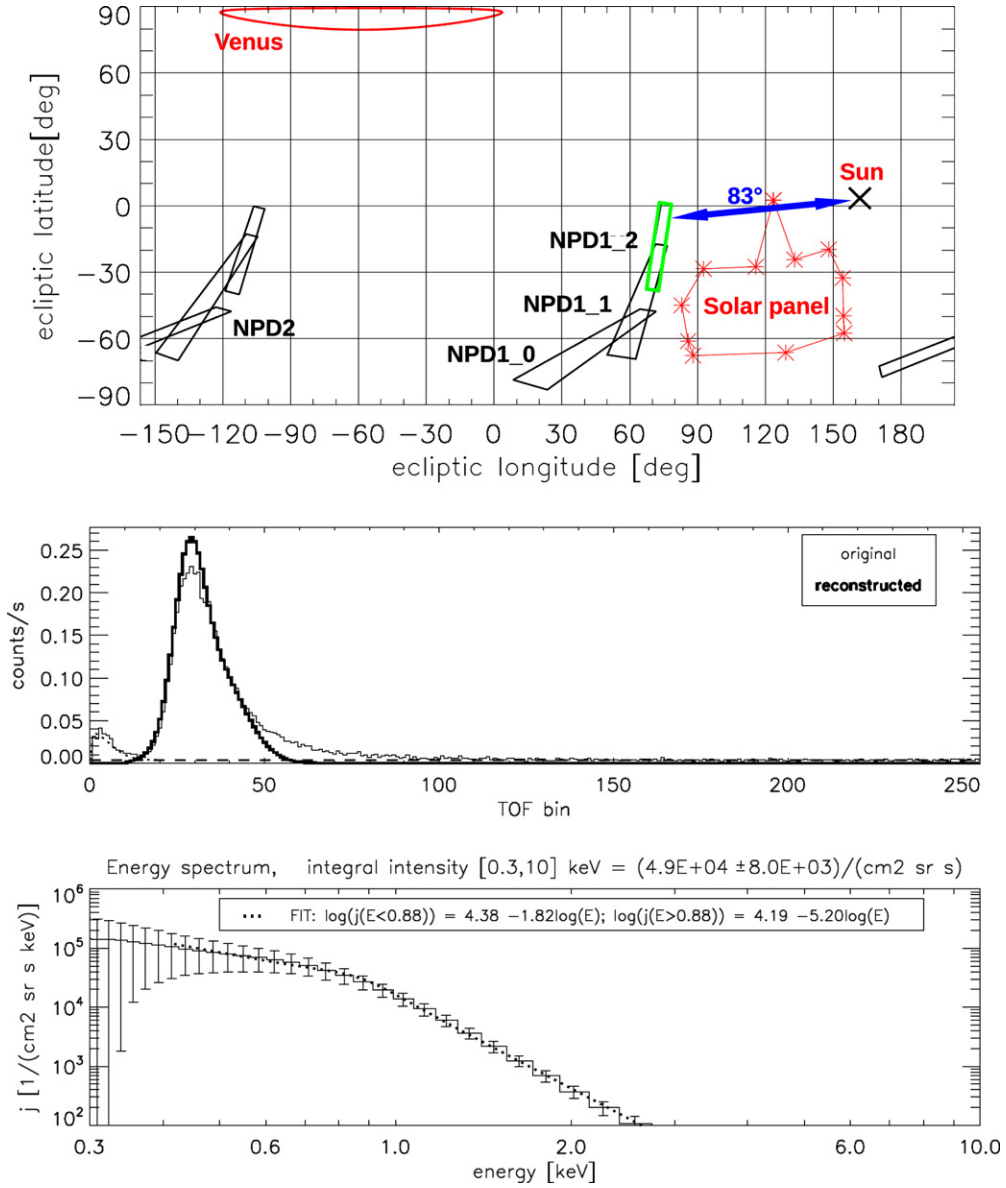

Figure 3. Neutralized solar wind entering sector NPD1_2 (marked green in the top panel) on 2006 June 5. Same format as Figure 2. This ENA signal was created by solar wind protons neutralized at the entrance slit of the NPD sensor. A flat low-energy slope (−1.82) is followed by a very steep power law of −5.2 at energies >0.88 keV.

(A color version of this figure is available in the online journal.)

After applying all exclusion criteria, we kept a set of 149 independent observations, each of them lasting between 10 minutes and 2 hr. This data set includes 134 observations from ASPERA-4/NPD and only 15 from ASPERA-3/NPD. Once *MEX* was in orbit (from 2004 February onward), the broad spatial distribution of planetary ENAs around Mars (Galli et al. 2008b) made the study of the faint non-planetary ENAs impossible. For ASPERA-4 on *VEX*, on the other hand, plenty of observations from the orbit apocenter at 60,000 km altitude were found suitable. We included all ASPERA-4/NPD data obtained in Venus's orbit from 2006 May to 2007 December. Figure 5 shows the selected data as retrieved ENA intensities against time (in years since 2003 January 1). Note the gap in observations of 2 yr between the ASPERA-3 and ASPERA-4 data sets.

2.3. Conversion of Count Rates into Intensity Spectra

We converted the raw count rates of an ENA signal (the TOF spectrum in the middle panel in Figure 2) into differential intensity j in units of cm^{-2} sr^{-1} s^{-1} keV^{-1} (bottom panel in Figure 2) assuming that the signal was only produced by hydrogen atoms between 0.3 keV and 10 keV. As a first step, we subtracted the background caused by UV photons (dashed line in the middle panel of Figure 2) and the irregular peak caused by instrument electronics (dotted line in first TOF bins of same panel). The UV background was fitted by linear regression from the count rates in TOF bins where no ENAs are expected (TOF bins 100–256) and was then subtracted from the TOF peak produced by ENAs. The irregular peak was fitted by a Gaussian or by an exponential decrease. If the ENA signal, after background subtraction, depended on the noise model used for the irregular peak, the error bars of the intensity and of the spectrum parameters were increased accordingly. If the ratio between the low-frequent ENA signal and the high-frequent noise was larger than 10 (evaluated in Fourier space), we considered this as distinct ENA signal with an integral intensity $J > 0$. Otherwise, J was set to zero and its upper limit was

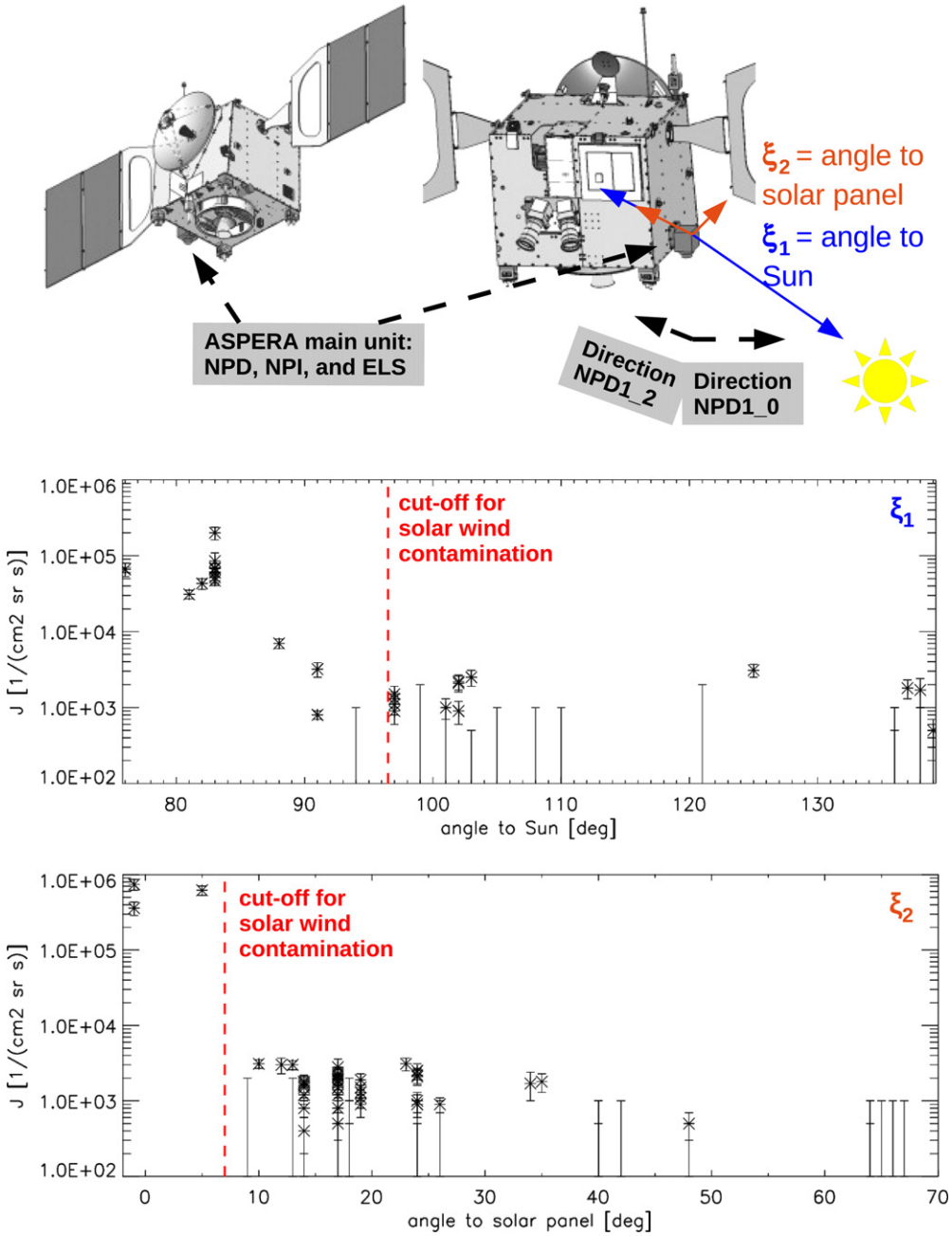

Figure 4. Uncorrected ENA intensities vs. spacecraft related angles. Only NPD1/ASPERA-4 data from 2006 were included. Top panel: *VEX* spacecraft with ASPERA-4 main unit (dark gray box). Middle panel: intensity vs. minimum angle between FOV and Sun; bottom panel: intensity vs. angle between FOV and solar panel. Dashed lines indicate the cutoff angles for uncontaminated data.

(A color version of this figure is available in the online journal.)

derived by interpreting every count rate above the background as valid ENA signal. The measured TOF spectrum caused by ENAs has to be understood as the convolution of the original TOF distribution with the instrument response. The latter is an asymmetric peak, approximated by the sum of a Gaussian and a Lorentzian profile, with $\Delta E/E = 0.45$ for all energies between 0.3 and 5.0 keV (Grigoriev 2007). We used a least-square fitting method to reconstruct the original TOF distribution without the effects of the instrument response function. The result of this inversion is the reconstructed TOF spectrum, shown as thick black line in the middle panel of Figure 2. The parts of the TOF spectrum that corresponded to energies above 20 keV or below 0.2 keV were discarded since the instrument efficiencies are known only for the energy range 0.3–5 keV. As the last step, the reconstructed TOF spectrum $C_{\rm rec}$ was converted into differential intensities j (bottom panel of Figure 2) via Equation (2):

$$j = \frac{C_{\rm rec}}{G_0 \epsilon(E) r(E)}. \quad (2)$$

In Equation (2), ϵ denotes the energy-dependent detection efficiency, G_0 is the geometrical factor, and $r(E)$ is the corresponding energy range of the TOF bin. Because the energy resolution at a given energy is much coarser than $r(E)$, the degree of freedom of the retrieved spectrum is much smaller than the number of 256 different TOF bins. Theoretically, up to 10 independent spectrum parameters could be retrieved for a strong hydrogen ENA signal. Since the non-planetary signals presented in this

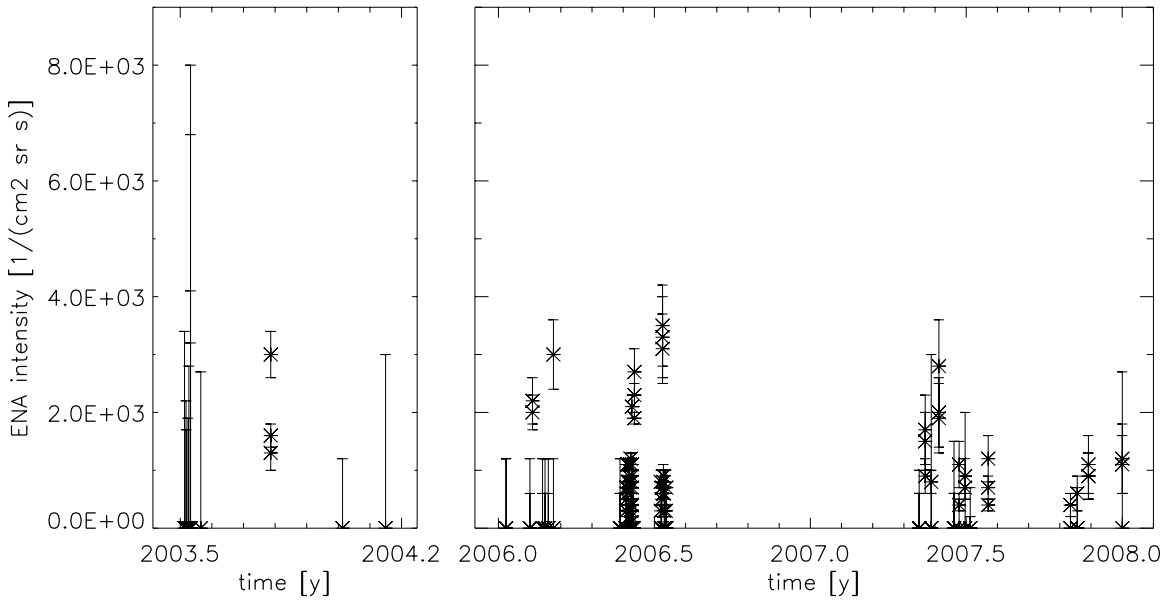

Figure 5. Observation times of all non-planetary ENA measurements with ASPERA-3 (left panel) during the cruise phase to Mars and with ASPERA-4 in the vicinity of Venus (2006 and 2007, right panel).

analysis are close to the detection threshold, we described j with only four parameters by Equations (3a) and (3b):

$$j = j_1 \left(\frac{E}{E_0}\right)^{\alpha_1}, \; E < E_k \tag{3a}$$

$$j = j_2 \left(\frac{E}{E_0}\right)^{\alpha_2}, \; E > E_k. \tag{3b}$$

The parameters α_1 and α_2 denote the spectral slopes at low and high energies, respectively, and E_k is the position of the knee between low and high energies. The fourth parameter is the intensity $J = \int j dE$ in units of $\mathrm{cm}^{-2}\ \mathrm{sr}^{-1}\ \mathrm{s}^{-1}$, integrated from 0.3 to 10 keV for uncorrected signals and from 0.4 to 5 keV for corrected signals. Deviations from this simple two-component power law were sometimes visible, such as the slight curvature at low energies in the bottom panel of Figure 2. However, the uncertainty of the corresponding fit parameter was too large for quantitative analysis.

The energy range is determined by the sensitivity of the instrument. For energies below 0.3 keV, the error bars of retrieved intensities usually are larger than the intensity itself because the detection efficiency is low and not well known. For energies above 10 keV, counting statistics are insufficient and the uncertainty introduced by the irregular peak at the first TOF bins becomes too large. The integral intensity turned out to be the most robust parameter for measurements with a low signal-to-noise ratio (see Section 3). If the error bars of the retrieved α_1, α_2, and E_k were larger than the values, the latter were omitted from analysis.

The NPD/ASPERA-4 observations obtained after 2006 June had to be corrected for the degrading detection sensitivity caused by the intense UV light reflected off Venus's atmosphere. The upper panel of Figure 6 shows that the uncorrelated start count rates of the sensor continually dropped after from 2006 May onward. Only data corresponding to non-planetary ENA observations with a distinct ENA signal are included in this figure, but the temporal evolution of sensor count rates follows the same trend for all NPD/ASPERA-4 observations. This decrease of detection efficiency results in apparently decreasing ENA intensities, illustrated in the lower panel. The red lines in Figure 6 indicate the linear regression plus its 1σ uncertainty over the time span from 2006 July to 2007 December. For evaluation, ENA intensities measured after 2006 June were multiplied by the inverse of this linear fit. For the data points in 2006 July, the correction factor calculated to 1.15 ± 0.1. For 2007 March to May, it increased to 1.65 ± 0.5 and to 2.2 ± 1.1 for 2007 September to December. These factors did not notably change between individual sectors of NPD1 or for different region in the sky. Since the error bar of the correction factors increased with time, the relative uncertainty of corrected ENA intensities increased from typically 20% relative error (2006 July) to 50% relative error by the end of 2007. This is the reason why we excluded data after 2007 from analysis. To derive these correction factors, we assumed that the intensity of the heliospheric ENAs did not vary during the 1.5 yr of observation times. The all sky ENA fluxes measured with *IBEX*-Hi varied by 20% or less from 2009 to 2011 (McComas et al. 2012), but those measurements were obtained at a different time of the solar cycle (see, e.g., Zank et al. (2010) for a model of heliospheric ENA variability with solar cycle). We therefore verified that we obtained the same correction factors when analyzing the temporal decrease of other signals, such as neutralized solar wind or planetary ENAs.

After having derived ENA intensities, two further steps were necessary to compare the results to measurements from other instruments. First, the apparent intensities were corrected for the survival probability of a hydrogen ENA against ionization by charge exchange with the solar wind or due to photoionization. This calculation was made under the assumption that the ENAs originated from the heliosheath with a fixed travel distance of 90 AU. The calculation was done separately for every observation direction and for every energy bin, with the energies corresponding to the spacecraft reference frame (see details in Appendix 2 of McComas et al. 2012). The survival probabilities for the paper by McComas et al. (2012) and for the present study were calculated using the same homogeneous model of solar wind evolution in time and heliolatitude and of the solar EUV output. The survival probability analysis is thus identical for the two studies. The solar factors contributing to

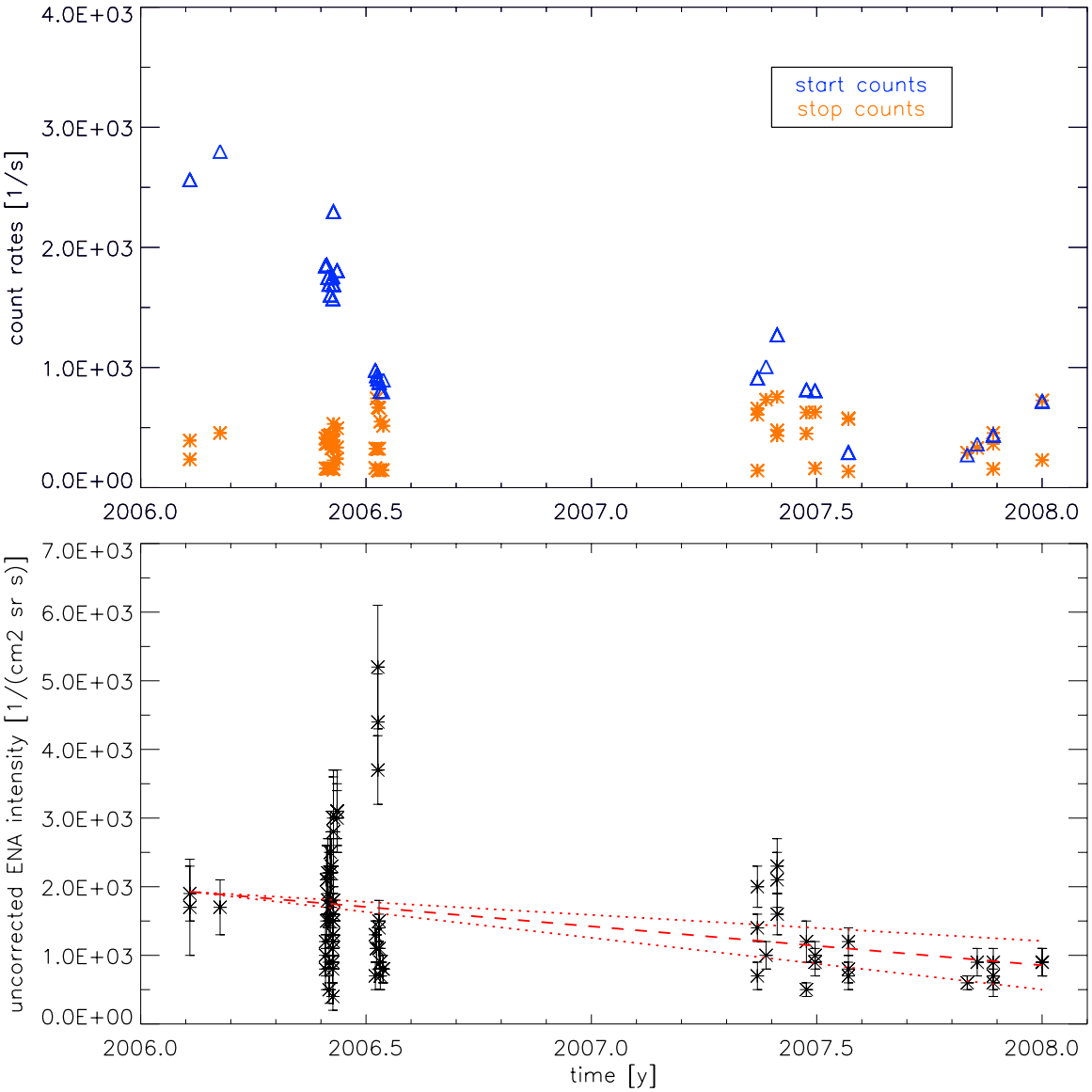

Figure 6. Decreasing detector sensitivity of NPD/ASPERA-4 with time. The upper panel shows uncorrelated start (triangles) and stop count rates (asterisks) of NPD1, the lower panel shows ENA intensities without any corrections for sensor degradation, Compton–Getting, or survival probability. The red lines indicate the linear regression through all data points with the corresponding 1σ uncertainty.

(A color version of this figure is available in the online journal.)

the survival probabilities are discussed by Bzowski et al. (2013) and Sokółet al. (2013). ENAs close to the ecliptic plane (i.e., from the nose or the tail of the heliosheath) have a lower survival probability than ENAs coming from high heliolatitudes. Most of the ENA losses occur within the innermost 10 AU to the Sun because the effective ionization rate for a given energy decreases with the square of solar distance.

Since only observations from the Sun-far hemisphere were included and because the minimum detectable ENA energy was 0.3 keV, the effect of the loss correction on ENA intensities was moderate. For the NPD/ASPERA-4 observations in the vicinity of Venus, the intensity correction averaged to a factor of 1.64 ± 0.13. For the NPD/ASPERA-3 observations, the correction factor was 1.31 ± 0.05. The uncertainty of these loss corrections is smaller than 6% for NPD/ASPERA-3, and smaller than 12% for NPD/ASPERA-4 observations (energies $\geqslant$0.3 keV). These uncertainties were negligible compared to the measurement uncertainties.

Second, we corrected for the Compton–Getting effect caused by the motion of the spacecraft relative to the viewing direction (McComas et al. 2010). If the velocity vector of the spacecraft in the inertial ecliptic reference frame is given by $\mathbf{u}$ ($u_z = 0$ for motions close to the ecliptic plane), the measured velocity $\mathbf{v}_\mathrm{m}$ of an incoming ENA with velocity $\mathbf{v}_\mathrm{i}$ is

$$\mathbf{v}_\mathrm{m} = v_\mathrm{m} \begin{pmatrix} \cos\lambda_\mathrm{m} \cos\beta_\mathrm{m} \\ \sin\lambda_\mathrm{m} \cos\beta_\mathrm{m} \\ \sin\beta_\mathrm{m} \end{pmatrix} = v_\mathrm{i} \begin{pmatrix} \cos\lambda_\mathrm{i} \cos\beta_\mathrm{i} \\ \sin\lambda_\mathrm{i} \cos\beta_\mathrm{i} \\ \sin\beta_\mathrm{i} \end{pmatrix} + \begin{pmatrix} u_\mathrm{x} \\ u_\mathrm{y} \\ 0 \end{pmatrix}, \quad (4)$$

with λ and β being the ecliptic longitude and latitude. Thus, the energy in the inertial reference frame $E_\mathrm{i} = (m/2)v_\mathrm{i}^2$ is related to the measured energy $E_\mathrm{m} = (m/2)v_\mathrm{m}^2$ by

$$E_\mathrm{i} = E_\mathrm{m} \left(1 + \frac{mu^2}{2E_\mathrm{m}} - \sqrt{\frac{2m}{E_\mathrm{m}}} \cos\beta_\mathrm{m} (u_\mathrm{x} \cos\lambda_\mathrm{m} + u_\mathrm{y} \sin\lambda_\mathrm{m}) \right). \quad (5)$$

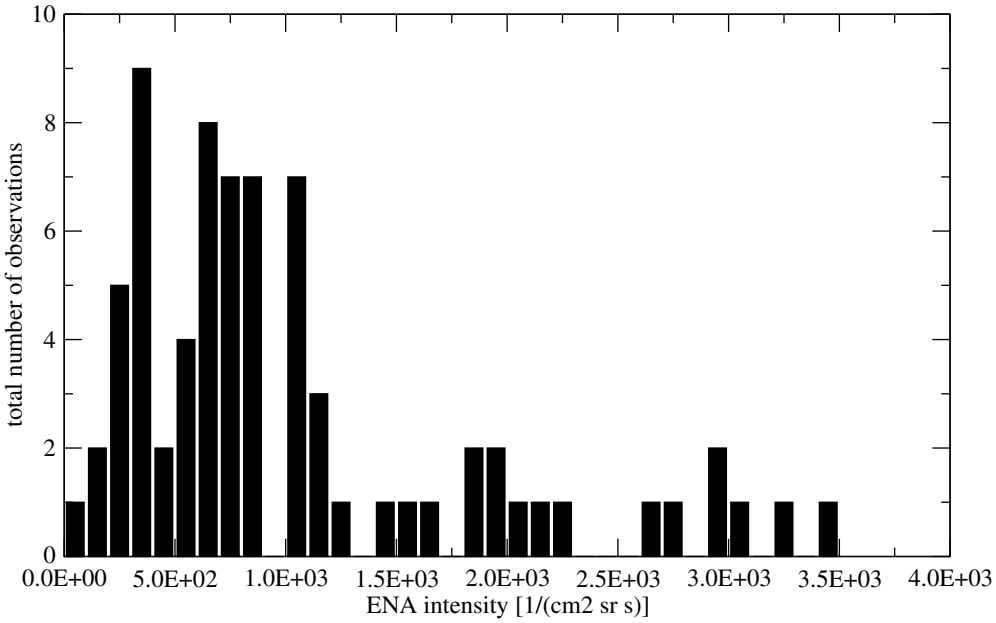

Figure 7. Histogram of corrected ENA intensity (integrated from 0.4 to 5 keV) for all 73 observations with a distinct ENA signal. The median value is 0.8×10^3 cm^{-2} sr^{-1} s^{-1}.

The ENA intensity in the inertial reference frame j_i was then evaluated—assuming invariance of phase-space density—as $j_i = j_m E_i / E_m$ for each energy bin of the spectrum. Since the magnitude of the spacecraft velocity u was 35 km s^{-1} at most, and the lowest ENA energy considered here (0.3 keV) corresponded to $v_i = 240$ km s^{-1}, the correction factor in Equation (5) varied between 0.75 and 1.3. For higher ENA energies, Compton–Getting becomes less important. Because the observed intensity was a strong function of energy (see Figure 2), this correction altered the integral intensities by a factor of two in the most extreme cases. Correcting for Compton–Getting also forced us to restrict the analysis to the energy range of 0.4 keV to 5 keV in the inertial reference frame. Otherwise data points at apparent energies below 0.3 keV would be included, for which the calibration uncertainty is larger than the values themselves.

On the other hand, the effect of Compton–Getting on the direction of ENAs was neglected. It amounted to a deflection of eight degrees at most, which is less than the FWHM of an NPD FOV. In the following sections, all results will be based on intensities corrected for survival probabilities and for Compton–Getting, unless the intensities are described as "uncorrected." By default, the results will be presented in intensity integrated over the entire sensitivity range of ASPERA-NPD. Differential intensities in units of cm^{-2} sr^{-1} s^{-1} keV^{-1} are reserved to plots of energy spectra (see for instance Figure 12).

3. RESULTS

The average and the standard deviation of the non-planetary ENA intensity observed with NPD/ASPERA calculate to 0.8×10^3 cm^{-2} sr^{-1} s^{-1} between 0.4 and 5.0 keV (Figure 5), including the entire database of 149 measurements. This indicates that the ENA signal is close to the detection limit of the NPD/ASPERA sensors. Out of the 149 measurements, 76 showed no distinct ENA signal. They correspond to those data points in Figure 5 with only the upper σ_J larger than zero. By default, these data points were interpreted as signals with intensity 0.5 times the upper limit when we calculated average intensities, but we also calculated averages omitting these measurements. The data points are not symmetrically distributed around the average. The error intervals that cover 68% of the data below and 68% of the data points above the average intensity calculate to $J = (0.8^{+1.0}_{-0.5}) \times 10^3$ cm^{-2} sr^{-1} s^{-1}. If we interpret measurements without detectable signals as $J = 0$, the average intensity reduces to $J = 0.5 \times 10^3$ cm^{-2} sr^{-1} s^{-1}. The histogram in Figure 7 gives an overview of all measurements with a distinct ENA signal. Here, the median and the standard deviation calculate to 0.8×10^3 cm^{-2} sr^{-1} s^{-1}, whereas the average increases to $J = 1.1 \times 10^3$ cm^{-2} sr^{-1} s^{-1}.

No trend of integral ENA intensities versus observation time is visible in Figure 5. For ENA intensities measured with *IBEX*-Hi, McComas et al. (2012) report a temporal variability of up to 20% over 3 yr. We cannot disentangle potential temporal from spatial variability in our limited data set. Moreover, we corrected the intensity of observations made in 2007 based on the assumption that the heliospheric signal is constant with time. The only meaningful check for temporal variability therefore is the comparison between ENA intensity measured before 2005 with ASPERA-3 on *MEX* and the one measured in 2006 with ASPERA-4. For ASPERA-3, the average ENA intensity and its standard deviation calculate to 1.8×10^3 cm^{-2} sr^{-1} s^{-1} and 1.0×10^3 cm^{-2} sr^{-1} s^{-1}, for ASPERA-4 the corresponding values are 0.7×10^3 cm^{-2} sr^{-1} s^{-1} for the mean and for the standard deviation. The ENA signal may have been two times more intense in 2003 than 3 yr later, but the alternative assumption that it is constant with time cannot be ruled out. The error spread of ASPERA-3 measurements is larger because of the higher detection limit and because of the viewing direction. During cruise phase to Mars, the NPD FOV was directed at the galactic center (black pixels at $\lambda = 240°$, $\beta = -30°$ in Figure 8). This led to an elevated UV background level that masked any potential ENA signal.

In Figures 8 and 9, we mapped the integral ENA intensities against ecliptic coordinates. The upper panel of Figure 8 shows the integral intensities from 0.4 to 5 keV for the entire data set after correcting for survival probabilities and Compton–Getting effect. All sky regions show similarly low ENA intensities of

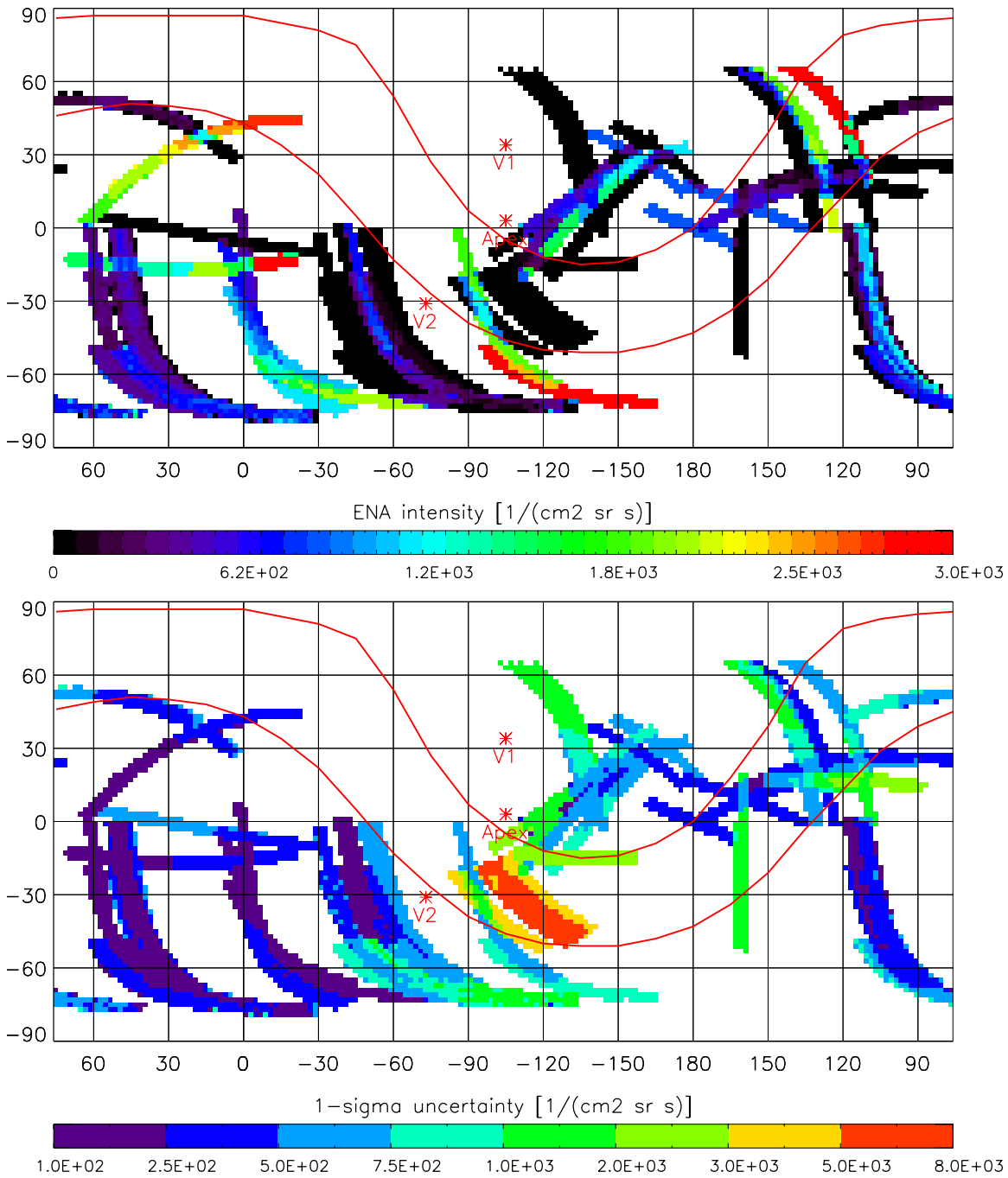

Figure 8. Spatial distribution of integral ENA intensities from 0.4 keV to 5 keV, plotted in inertial ecliptic reference frame. All observations were included, the black swaths correspond to measurements without a distinguishable ENA signal. The lower panel shows the corresponding 1σ uncertainties.

(A color version of this figure is available in the online journal.)

10^3 cm^{-2} sr^{-1} s^{-1} or no detectable ENA signal (black pixels). The positions of *Voyager 1* and *Voyager 2* and the apex direction of the interstellar gas flow are added as red asterisks. The two red curves show the geographic limits of the ribbon (refer to Figure 9) for which the *IBEX* sensors measured a two times more intense ENA signal than the average over the remaining sky. The lower panel indicates the uncertainty of these intensities. Figure 9 shows the spatial distribution of differential ENA intensities at 2.7 keV. The upper panel represents the ASPERA data set, excluding all zero measurements, the lower panel shows the map obtained with *IBEX*-Hi from 2009 to 2011 (McComas et al. 2012). The values in the upper panel are corrected for survival probabilities and Compton–Getting effect, whereas the intensities in the lower panel are only corrected for survival probability. However, at energies larger than 1 keV, the Compton–Getting correction changes the signal by less than 10%.

Two things are obvious from comparing the two panels in Figure 9. First, the differential intensities of ENAs at 2.7 keV agree within 50% between ASPERA and *IBEX*. Second, the coverage of the ASPERA data set does not allow to identify spatial structures. The only region that was observed by ASPERA many times with low uncertainty (see Figure 8) coincides with the "Region 4" of low ENA intensities seen

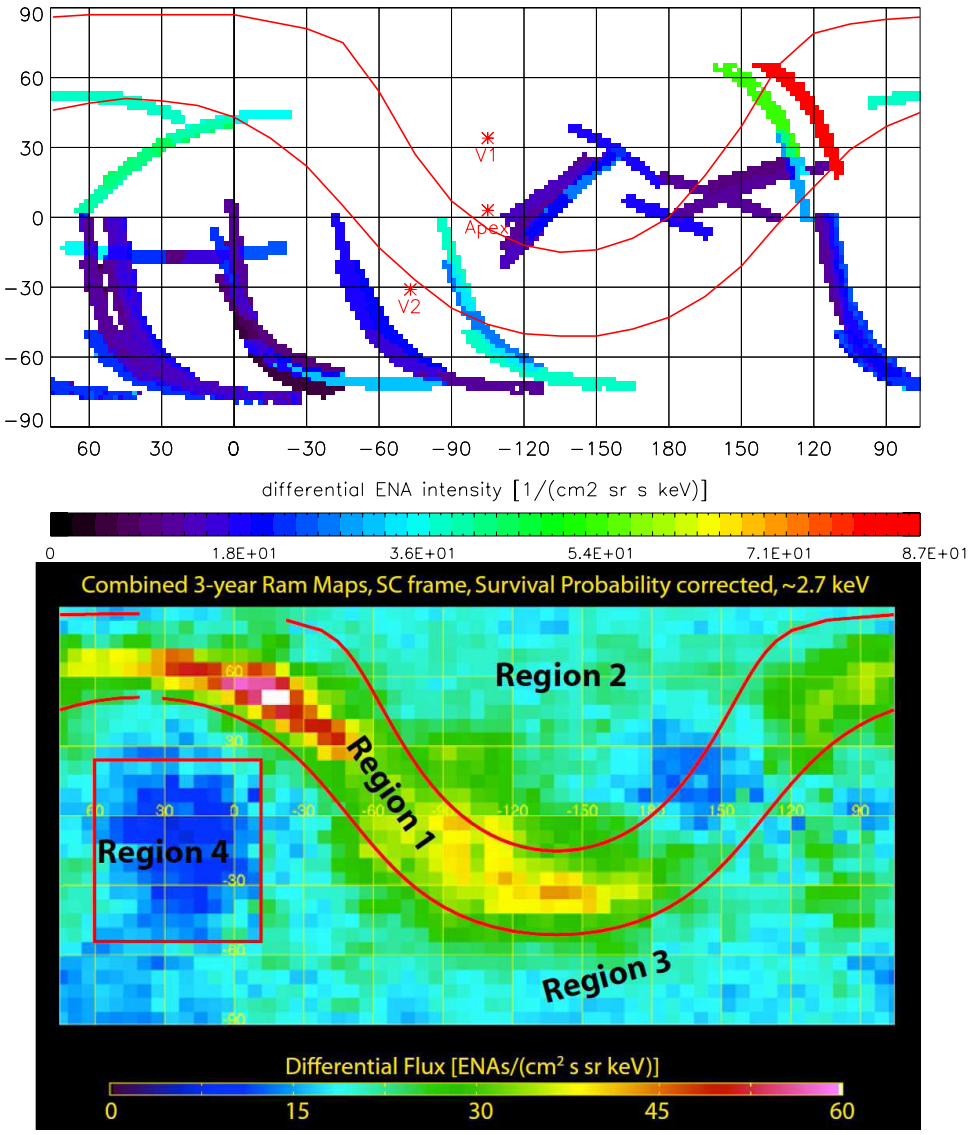

Figure 9. Spatial distribution of ENA intensities in ecliptic coordinates. The upper panel shows the differential intensity of the ENA signals observed with ASPERA, evaluated at 2.7 keV. Only measurements with a distinguishable signal were included. The red asterisks denote the direction of *Voyager 1*, *Voyager 2*, and the apex direction ($\lambda = 255°$, $\beta = 5°$). The limits of the ribbon of higher ENA intensities seen with *IBEX*-Hi are sketched in red. The lower panel is a reprint of Figure 24 from McComas et al. (2012), which summarizes the *IBEX*-Hi results for energy channel 5 at 2.7 keV.

(A color version of this figure is available in the online journal.)

with *IBEX*. For ASPERA, the average corrected ENA intensity inside the ribbon is higher by a factor of 1.7 than outside, but this difference is not statistically significant: 34 measurements (including measurements without detectable signal) fall inside with an average of 1.2×10^3 cm^{-2} sr^{-1} s^{-1} and a standard deviation of 1.0×10^3 cm^{-2} sr^{-1} s^{-1}, whereas the signals outside the ribbon have an average and standard deviation of 0.7×10^3 cm^{-2} sr^{-1} s^{-1}. Over the same energy range, *IBEX* measured an intensity of 0.8×10^3 cm^{-2} sr^{-1} s^{-1} for the ribbon (Table 2 in Fuselier et al. 2012), and 0.4×10^3 cm^{-2} sr^{-1} s^{-1} for the *Voyager 2* direction outside the ribbon (Table 4 in Fuselier et al. 2012). This is consistent with a heliospheric origin of the ENA signals observed with ASPERA. However, the observations are too sparse and the statistical scatter (see lower panel of Figure 8) is too large to verify the ENA ribbon detected with *IBEX*. Likewise, not enough signals with an identifiable spectrum were detected to organize the spectral parameters with respect to the direction in the sky. Since neither intensities nor spectral parameters allow to reliably identify different sky regions, we averaged the intensity and the spectral parameters of the ENA signal over all directions.

For the most intense ENA signals, the three spectral parameters α_1, α_2, and E_k (Equations (3a) and (3b)) could be fitted with a relative error smaller than 20%. Weaker signals corresponded to a flat, featureless TOF spectrum for which only the low-energy slope was fitted. An analysis of the retrieved spectral parameters revealed, however, that this slope was not trustworthy for weak ENA signals. This is demonstrated in Figure 10, top panel. Below an apparent intensity of 3×10^3 cm^{-2} sr^{-1} s^{-1}, all retrieved slopes fall below the dashed line ($\alpha_1 = -2.9$), which is predicted for a completely flat TOF signal. This implies that the spectrum of an ENA signal close to the detection threshold is dominated by the instrument properties. We therefore decided to estimate the average α_1 from the data points with apparent intensities $J > 3 \times 10^3$ cm^{-2} sr^{-1} s^{-1} (black lines in the top panel of Figure 10). Most estimates for the knee E_k (middle panel) and the high-energy slope α_2 (bottom panel) were derived for ENA signals $J \geqslant 2 \times 10^3$ cm^{-2} sr^{-1} s^{-1}. No dependence with

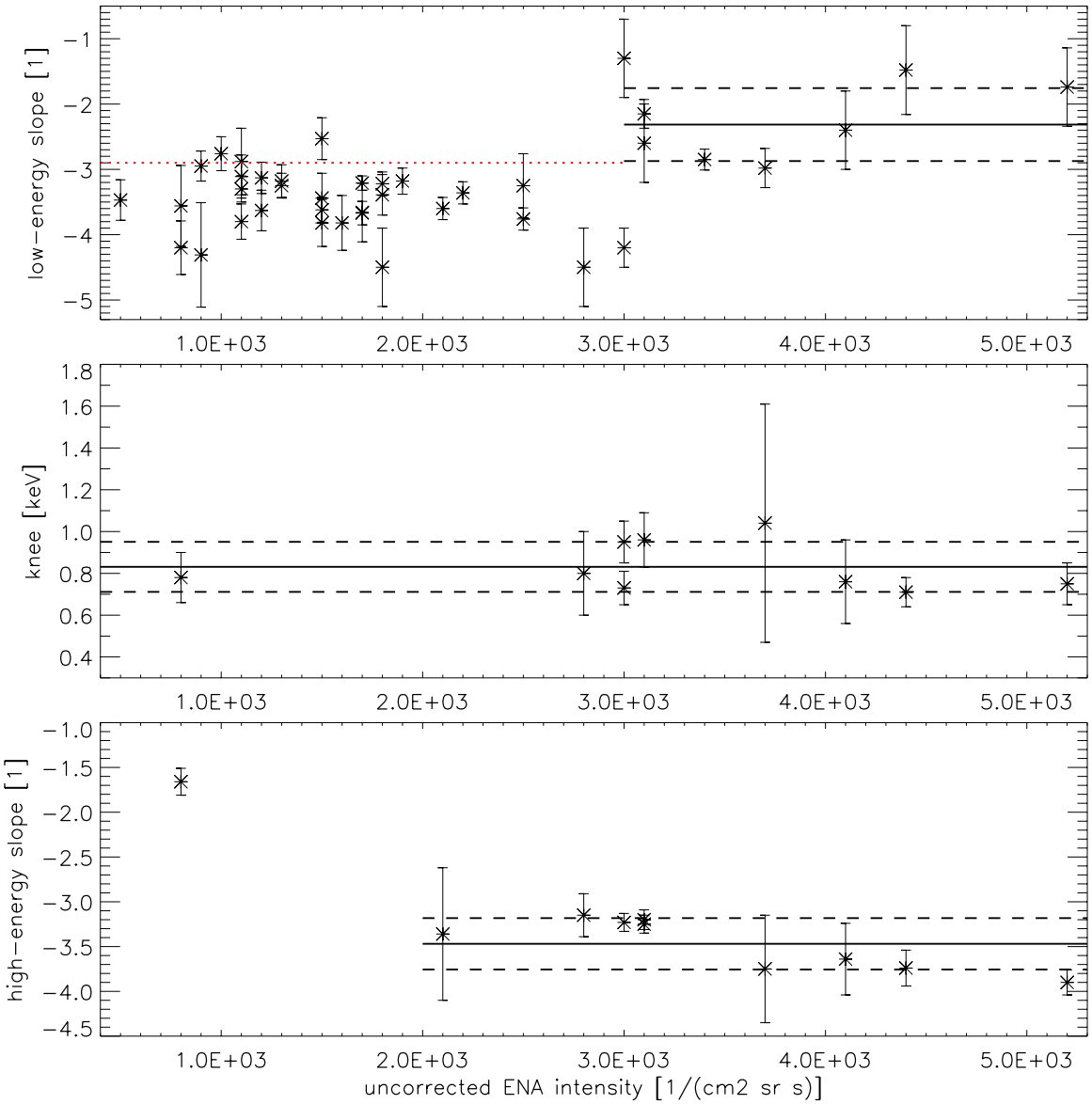

Figure 10. Derived energy spectrum parameters (see Equations (3a) and (3b)) vs. apparent ENA intensity. Solid and dashed black lines indicate the mean and the standard deviation of measurements. Top panel: low-energy power-law exponent α_1, red dotted line at $\alpha_1 = -2.9$ indicates slope expected for a completely flat TOF spectrum. Middle panel: position of knee E_k (keV). Bottom panel: high-energy power-law exponent α_2.

(A color version of this figure is available in the online journal.)

Table 1
ENA Spectrum Parameters from ASPERA and *IBEX*-Hi (McComas et al. 2012)

	Energy Range	Intensity (cm^{-2} sr^{-1} s^{-1})	Low-energy Power Law	Knee (keV)	High-energy Power Law
NPD/ASPERA, overall average	0.4 to 5 keV	$(0.8^{+1.0}_{-0.5}) \times 10^3$	-2.3 ± 0.6	0.83 ± 0.12	-3.5 ± 0.3
IBEX, ribbon	0.5 to 6 keV	$(0.5 \pm 0.1) \times 10^3$	N/A	N/A	-2.1 ± 0.3
IBEX, *Voyager 2*	0.5 to 6 keV	$(0.3 \pm 0.1) \times 10^3$	N/A	N/A	-1.8 ± 0.3

apparent intensity or observation time was visible for the latter two spectral parameters. From Figure 10, the mean and the standard deviation of the three spectral parameters calculated to $\alpha_1 = -2.3 \pm 0.6$, $E_k = 0.83 \pm 0.12$ keV, and $\alpha_2 = -3.5 \pm 0.3$. These values are compared to *IBEX*-Hi results in Table 1. The values for *IBEX*-Hi are based on Figure 14 in McComas et al. (2012). We extracted the average differential intensity for each of the five *IBEX*-Hi energy channels for a 4×4 pixel region around the *Voyager 2* and ribbon direction by a graphics program. We then converted the five differential intensities into one integral intensity from 0.5 to 6 keV by multiplying each of the values by the range of the corresponding energy channel. The uncertainty stated in Table 1 is due to the intrinsic spatial variability of the ENA signal. The spectral slopes were calculated by fitting a simple power law through the five extracted data points. Our numbers (-1.8 ± 0.3 and -2.1 ± 0.3) agree with

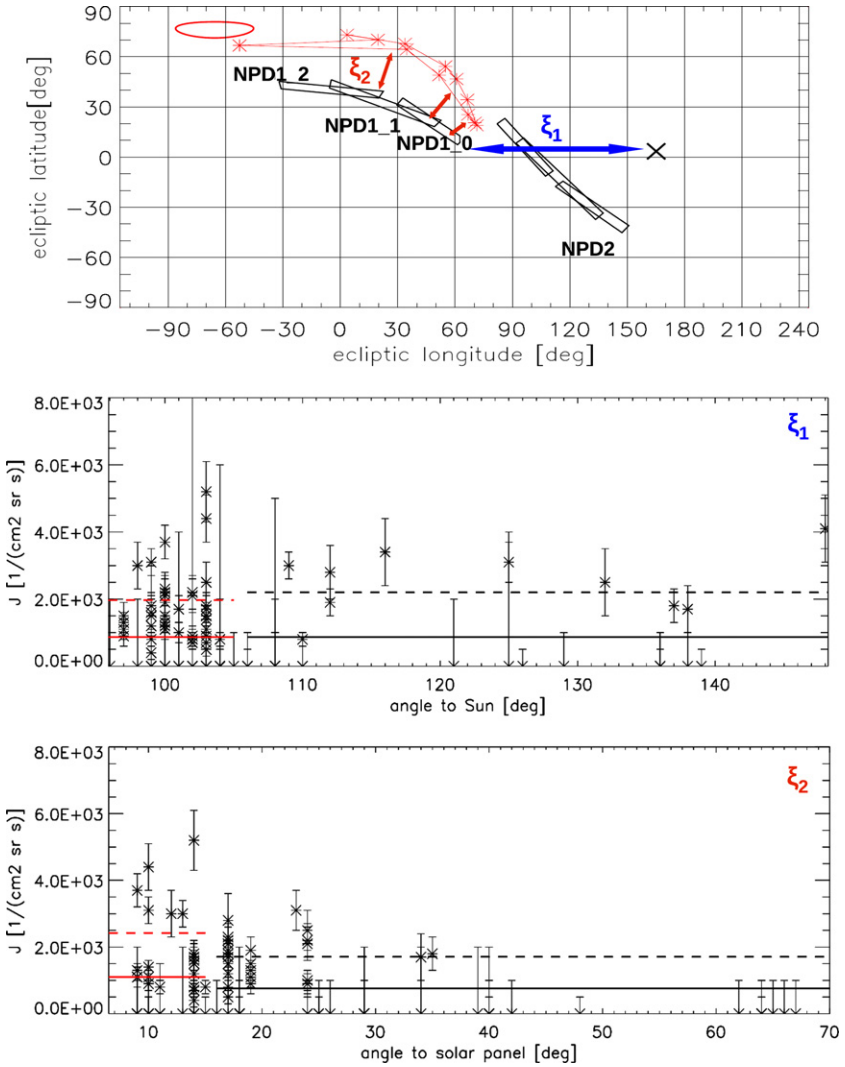

Figure 11. Uncorrected ENA intensities vs. spacecraft related angles, ASPERA-4 observations after 2006 were excluded. ξ_1: minimum angle between NPD FOV and Sun (middle panel). ξ_2: minimum angle between NPD sectors and solar panel (bottom panel). Solid and dashed lines denote average and standard deviations of intensities, respectively.

(A color version of this figure is available in the online journal.)

Figure 24 shown by McComas et al. (2012) and with the values −1.5 and −1.9 derived by Fuselier et al. (2012).

A large part of the analysis was dedicated to the exclusion of solar wind contaminated spectra (see Section 2). After having obtained the results in Table 1, we tested if the underlying data exhibit a correlation with angular distance to the solar wind ξ_1 or angle to the solar panel ξ_2. These angles are illustrated in the top panel of Figure 11. There, the apparent ENA intensity (i.e., without correction for Compton–Getting effect and re-ionization processes) is plotted against the instrument angles. For this test, ASPERA-4 data sampled after 2006 were excluded because of the decreasing detector sensitivity. The red and black lines in Figure 11 indicate the average and the standard deviation of the apparent ENA intensities. The data set was separated into angles ξ_1 below and above 105° (middle panel) and ξ_2 below and above 15° (bottom panel). The two ranges overlap in both cases, the apparent intensity at larger instrument angle is not significantly lower than for small angles. The same result is found for other angles as long as the number of measurements in both sub-divisions is much larger than one. Similarly, the results for average intensity and spectral parameters in Table 1 do not change if stricter filter criteria ($\xi_1 > 105°$, $\xi_2 > 15°$) are applied to the entire data set.

We also calculated the linear Pearson correlation coefficient r for both instrument angles. For the angle to the solar wind, it is very weak and not significant ($r = -0.03$). For the distance to the solar panel, r is rather weak (−0.3) but significant at a 98% level. It decreases to $r = -0.04$ if only non-zero measurements are taken into account, i.e., measurements with a TOF peak distinguishable against the background (see Section 2.3). The quality of this statistical analysis is limited by the small number of data. There are only eight independent measurements with a distance $\xi_2 > 45°$ to the solar panel. Moreover, seven of them were obtained when NPD was directed away from the ENA ribbon (see Figure 9). The apparent correlation of ENA intensity with distance to the solar panel may therefore be misleading. In any case, it cautions us to not rule out the possibility of solar wind contamination.

4. DISCUSSION

Direct comparison of the intensities in Table 1 to the previous results for ASPERA-3 (Galli et al. 2006a; Wurz et al. 2008)

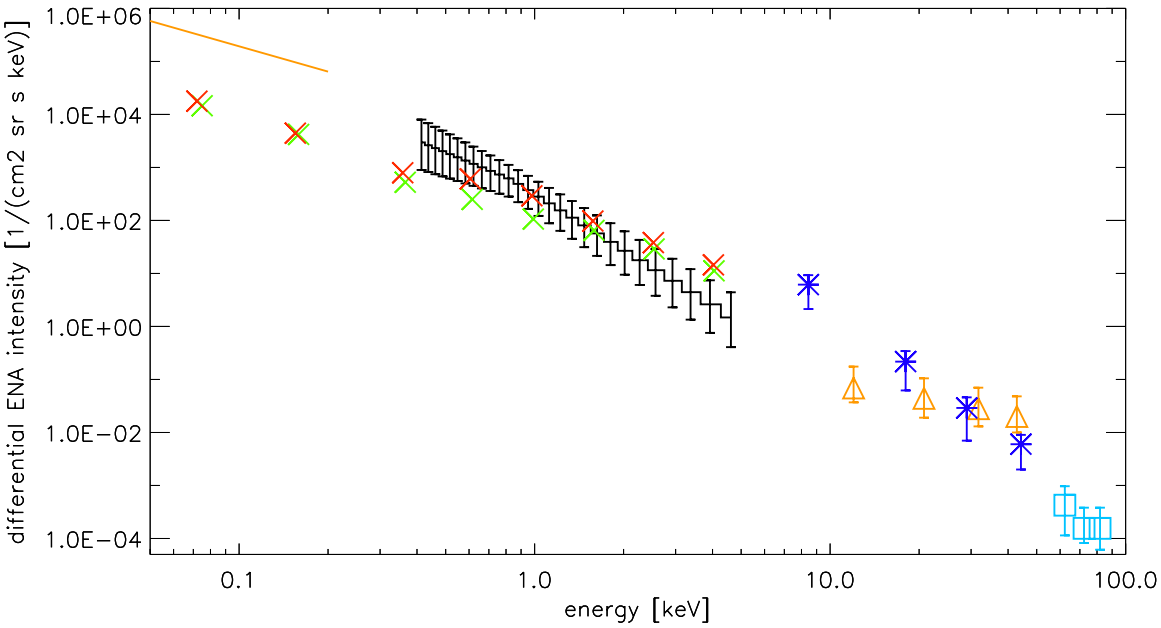

Figure 12. Comparison of various measurements of heliospheric ENA spectra. Black histograms with error bars: ASPERA (Table 1), crosses: loss-corrected ENA intensities measured with *IBEX* for *Voyager 2* (green) and ENA ribbon (red) directions (Fuselier et al. 2012). Orange line: upper limit on possible heliospheric ENAs (Wood et al. 2007). Blue asterisks: INCA/*Cassini* measurements for *Voyager 2* direction (Krimigis et al. 2009), orange triangles: upper limits on H-ENAs derived with HENA/*IMAGE* (Kallenbach et al. 2005), light blue boxes: HSTOF/CELIAS/*SOHO* data (Hilchenbach et al. 1998).

(A color version of this figure is available in the online journal.)

and for ASPERA-4 (Brandt et al. 2009) can be misleading since none of these publications included re-ionization losses. Moreover, Galli et al. (2006a) and Wurz et al. (2008) did not correct for the Compton–Getting effect, whereas Brandt et al. (2009) used a different energy range and no time-dependent detection efficiencies. Despite these differences we note that the average ENA intensity is one order of magnitude lower than reported in the two previous ASPERA-3 publications. There are two reasons, beside the different data analysis, for this decrease. The preliminary instrument calibration (before Grigoriev 2007) implied lower detection efficiencies (thus the reconstructed intensities were too high), and exclusion of contaminated data was less rigorous than in the present study. This concerns measurements made when the FOV was less than 97° away from Sun direction and data affected by outgassing. The ASPERA-4 intensities presented by Brandt et al. (2009) varied between 10^2 and 10^3 cm^{-2} sr^{-1} s^{-1}, integrated from 0.3 keV to 1.0 keV. This is the same order of magnitude as the loss-corrected ENA intensity in this study. The discrepancy in ENA intensity of one order of magnitude between previous ASPERA-3 and ASPERA-4 results has been resolved.

The average ENA intensity measured with ASPERA and the *IBEX*-Hi results published by McComas et al. (2012) agree for the overlapping energy range (see Table 1). A direct comparison between the two data sets is possible because McComas et al. (2012) relied on the same model to correct for re-ionization losses of heliospheric ENAs. For ASPERA, no statistically significant correlation of the ENA signal with sky regions is visible, whereas McComas et al. (2012) find higher intensities in the ribbon than in the surrounding regions. In Table 1 we noted the values for the ribbon and for *Voyager 2* direction. On the other hand, McComas et al. (2012) fit only a single power law to their energy spectra from 0.5 to 6 keV. They find a steeper power law $\alpha \leqslant -2.0$ in the ecliptic and $\alpha \geqslant -2.0$ toward the ecliptic poles.

The average ENA intensity and spectrum parameters listed in Table 1 were used to define the typical ASPERA energy spectrum of ENAs. Figure 12 juxtaposes this spectrum (black histogram) with other measurements of heliospheric ENAs in an inertial reference frame. The error bars of the ASPERA spectrum show the 1σ uncertainty of the two spectral slopes (-2.9 and -3.2 for the upper limit, -1.7 and -3.8 for the lower limit). The uncertainty of the knee is negligible for this plot. The integral intensity of the histogram corresponds to $J = 0.8 \times 10^3$ cm^{-2} sr^{-1} s^{-1}, the error bars were scaled by a constant factor to the lower and upper error limit of the integral intensity of 0.3×10^3 cm^{-2} sr^{-1} s^{-1} and 1.8×10^3 cm^{-2} sr^{-1} s^{-1} (Table 1). The crosses denote the two *IBEX* energy spectra for the *Voyager 2* (green) and the ENA ribbon (red) viewing direction (Fuselier et al. 2012). These spectra agree with the *IBEX*-Hi maps presented by McComas et al. (2012) who averaged measured ENA intensities over 3 yr of *IBEX* observations and corrected for Compton–Getting and survival probabilities. The location of the *Voyager 2* and ENA ribbon pixels were depicted in Figures 8 and 9. The other data sets in Figure 12 include the intensities measured with INCA/*Cassini* at the *Voyager 2* direction (Krimigis et al. 2009), and HSTOF/CELIAS/*SOHO* data (Hilchenbach et al. 1998). We added the upper limit on heliospheric ENAs derived by (Wood et al. 2007) from Lyα measurements and the upper limits at high energies derived with HENA/*IMAGE* (Kallenbach et al. 2005).

The spectrum obtained by ASPERA steepens at higher energies and is thus similar to the characteristic ribbon spectra observed by *IBEX* (e.g., Schwadron et al. 2011; Dayeh et al. 2012). The only difference between ASPERA and *IBEX* spectra in Figure 12 is the steeper spectral slope (-2 to -3 for NPD/ASPERA, -1 to -2 for *IBEX*) for energies above 1 keV. Note, however, that spectral slopes between -2 and -3 are also reported by McComas et al. (2012) for *IBEX*-Hi observations from the ecliptic regions. We verified that the spectral

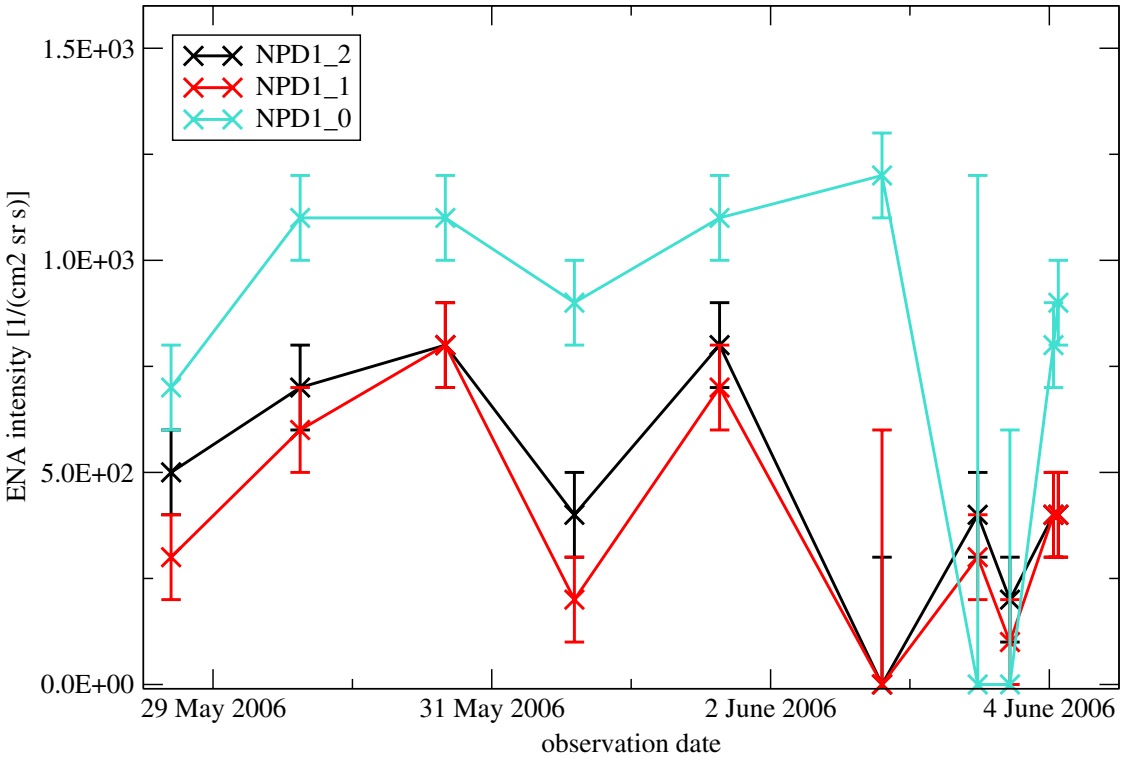

Figure 13. Temporal variability of measured ENA signal for one week of NPD/ASPERA-4 observations.
(A color version of this figure is available in the online journal.)

parameters derived from ASPERA and *IBEX* data can directly be compared with each other. Our method of converting the TOF spectrum into differential intensities (Equation (2)) is equivalent to the approach used by the *IBEX* team (Funsten et al. 2009). If the flat ENA energy spectrum ($\alpha \geqslant -2$) measured with *IBEX* at higher ecliptic latitudes is correct, a knee around 10 keV has to be postulated to bring the spectrum in agreement with the measurements at higher energies. The ASPERA spectrum is too low with respect to the lowest energy bin of the INCA/*Cassini* measurements, but the remaining data points are covered when the observed spectrum is extrapolated to higher energies. Moreover, the knee at 0.8 keV seems plausible for an ENA signal related to slow or shocked solar wind.

A pressure balance calculation in analogy to Schwadron et al. (2011) and Fuselier et al. (2012) for the ASPERA energy spectrum in Figure 12 yields a similar pressure as derived from *IBEX* measurements. The stationary pressure times the line-of-sight l,

$$P_{\rm st} \times l = \frac{4\pi}{3 n_{\rm H}} \int_{0.4\,{\rm keV}}^{5.0\,{\rm keV}} m v_0 \frac{j(E_0)}{\sigma_{\rm p}}\, dE_0, \qquad (6)$$

calculates to 70 pdynes cm^{-2} AU (7 pPa AU) over the entire energy range of NPD/ASPERA. In Equation (6), m and v_0 are the mass and velocity of a proton, the charge-exchange cross-section $\sigma_{\rm p} = 2 \times 10^{-15}$ cm^2 (Gruntman et al. 2001), the number density of neutral hydrogen $n_{\rm H} = 0.1$ cm^{-3} (Bzowski et al. 2008), and E_0 is the energy of the ion (and ENA) in the outer heliosphere. If the stationary pressure in *IBEX*-Hi energy channels 2–6 (covering an energy range from 0.5 to 6.0 keV) is summed, $P_{\rm st} \approx$ 50–60 pdynes cm^{-2} AU for *Voyager 1* and *Voyager 2* pointing direction and $P_{\rm st} \approx 100$ pdynes cm^{-2} AU for the ribbon of more intense ENA signals (Tables 2–4 in Fuselier et al. 2012).

An important part of the re-analysis of the non-planetary ENA signals was to rule out any non-heliospheric origin of the signal. Galli et al. (2006a) already excluded several other physical explanations for the ENA signals measured with ASPERA. They showed that the signal does not correlate with the Parker angle of the solar wind, thus ruling out protons from corotating interaction regions neutralized in the vicinity of the spacecraft. In general, the measured intensity in the order of 10^3 cm^{-2} sr^{-1} s^{-1} argues against protons in the inner solar system as the source, since the local neutral hydrogen density is too low.

The direct contamination of the non-planetary ENA signal from looking at the solar panel or from solar wind entering the aperture at angles close to 90° can be excluded due to our selection criteria (see Figure 4). The only possible source of solar wind contamination would be the combination of the two effects, i.e., neutralized solar wind scatters from the solar panel into the hemisphere above the spacecraft and enters the entrance slit at angles >10° outside the FOV. According to calibration, the instrument sensitivity to hydrogen ENAs drops to a few percent already at the edge of the FOV. However, if as little as 0.1% of the scattered particles from the solar panel (intensities $\approx 10^6$ cm^{-2} sr^{-1} s^{-1}) reach the conversion surface at much larger angles, they would mimic an ENA intensity on the order of the observed non-planetary ENA signal. To strictly rule out this possibility, we would require measurements where the entire NPD aperture would be more than 90° away from any part of the solar panel. Unfortunately, this is geometrically impossible for *VEX* (ξ_2 is always smaller than 70° in Figure 11). On *MEX*, NPD was not mounted on the same spacecraft side as the solar panel, but also for these observations the angular distance happens to be smaller than 90°.

The comparison between ENA intensities measured at Mars and at Venus argues against solar wind neutralized at the

spacecraft. The non-heliospheric ENA signals seen at a 90° angle to the Sun (as shown in Figure 3) are roughly four times more intense around Venus than around *Mars*. This is easily understandable because the solar wind flux is roughly four times larger at 0.7 AU than at 1.5 AU. Figure 5 shows that the corrected ENA intensities above the detection limit are not stronger close to Venus (2006 and 2007) than those measurements made in 2003 between Earth and *Mars*. Given the paucity of valid ASPERA-3/*MEX* data, this is an argument but no proof against solar wind contamination.

Galli et al. (2006a) argued that the temporal variability of measured ENA intensity was hard to reconcile with a heliospheric origin of the observed signal. At an ecliptic longitude of 90°, they reported intensities (integrated from 0.4 to 5 keV) ranging from zero (upper limit a few 10^3 cm^{-2} sr^{-1} s^{-1}) to 7×10^4 cm^{-2} sr^{-1} s^{-1}. The main reason for this large variability were the intense ENA signals with $J > 10^4$ cm^{-2} sr^{-1} s^{-1} caused by outgassing effects and solar wind neutralized at the spacecraft. In the database of the present study, the best available subset of observations to assess temporal variability are the 10 measurements shown in Figure 13. They were obtained with NPD/ASPERA-4 over one week in 2006. The viewing direction of the three NPD sectors moved by only 15° in ecliptic longitude around $\beta = 47°$, $\lambda = -44°$. The standard deviations of the intensities in Figure 13 calculate to 0.21, 0.23, and 0.18 times 10^3 cm^{-2} sr^{-1} s^{-1} for sectors NPD1_2, NPD1_1, and NPD1_0. This corresponds to a relative variability of roughly 40% for NPD1_2 and NPD1_1, and to 20% for NPD1_0. The uncertainty of the single measurements were estimated to 20% for NPD1_2, NPD1_1, and to 10% for NPD1_0. If the observed ENA signal was in truth constant over the one week of observation time, our error assessment of ENA signals close to the detection limit was too optimistic by a factor of two. On the other hand, the temporal variability no longer argues against a heliospheric origin of the ENAs detected with ASPERA. ENA intensity maps synthesized from *IBEX* data (Fuselier et al. 2012; McComas et al. 2012) also exhibit variations on the order of 50% between two adjacent pixels (∼6°) at some locations (see analysis of polar ENA signals by Allegrini et al. 2012 and Reisenfeld et al. 2012).

5. CONCLUSIONS

The ASPERA data set for heliospheric ENA signals is limited since the observation of interstellar ENAs is far away from the scientific scope of *MEX* and *VEX*. This study has included every data set for which no plausible physical reason exists to reject it. The observations show a diffuse non-planetary ENA signal close to the detection limit of NPD, on average 10^3 cm^{-2} sr^{-1} s^{-1} between 0.4 and 5 keV. The ENA intensities do not significantly vary over timescales of hours or years, spatial variabilities cannot be detected because of the limited coverage.

Previous studies on ENA signals measured with ASPERA-3 overestimated the intensity by one order of magnitude because of preliminary calibration and the inclusion of observations dominated by outgassing effects or solar wind neutralized on the spacecraft. The discrepancy between ASPERA-3 and ASPERA-4 measurements has been resolved. The loss-corrected ENA intensity measured with ASPERA from 0.4 to 5 keV is consistent with the heliospheric ENA intensities measured with *IBEX*. The observation range of heliospheric ENAs has been extended from Earth's orbit to Mars and Venus and to the years 2003–2007.

The ASPERA data exhibit a break in the energy spectrum above 0.8 keV to steeper slopes, which matches the slopes at higher energies from INCA/*Cassini* and HSTOF/CELIAS/*SOHO*. This energy spectrum is similar to the ENA ribbon spectra measured with *IBEX*. The spatiotemporal coverage of ASPERA data and the sensitivity of the sensor are unfortunately insufficient to confirm the ribbon-like structure seen by *IBEX*. We cannot strictly rule out that the signal observed with ASPERA and the derived energy spectrum is affected by ions neutralized on the spacecraft. In this case, the signal presented here would have to be interpreted as upper limit of heliospheric ENAs in the years from 2003 to 2007.

For planetary observations, which are the main scientific objective of NPD/ASPERA, the present study is also important. It shows that non-planetary background ENA sources can be reduced to intensities of 10^3 cm^{-2} sr^{-1} s^{-1}. This is orders of magnitude weaker than ENA signals from Mars or Venus (Galli et al. 2008a, 2008b).

REFERENCES

Allegrini, F., Bzowski, M., Dayeh, M. A., et al. 2012, ApJL, 749, L41
Barabash, S., Lundin, R., Andersson, H., et al. 2006, SSRv, 126, 113
Barabash, S., Sauvaud, J.-A., Gunell, H., et al. 2007, P&SS, 55, 1772
Brandt, P. C., Roelof, E. C., Decker, R., et al. 2009, in AIP Conf. Proc. 1183, Shock Waves in Space and Astrophysical Environments, ed. X. Ao, H. Burrows, & G. P. Zank (Melville, NY: AIP), 102
Burlaga, L. F., Ness, N. F., Acuña, M. H., et al. 2008, Natur, 454, 75
Bzowski, M., Möbius, E., Tarnopolski, S., Izmodenov, V., & Gloeckler, G. 2008, A&A, 491, 7
Bzowski, M., Sokół, J. M., Tokumaru, M., et al. 2013, in Cross-Calibration of Far UV Spectra of Solar System Objects and the Heliosphere, ISSI Scientific Report Ser. 13, ed. E. Quémerais, M. Snow, & R. M. Bonnet (New York: Springer Science and Business Media), 67
Chalov, S. V., Fahr, H. J., & Izmodenov, V. V. 2003, JGR, 108, 1266
Dayeh, M. A., McComas, D. J., Allegrini, F., et al. 2012, ApJ, 749, 50
Funsten, H. O., Allegrini, F., Bochlser, P., et al. 2009, SSRv, 146, 75
Fuselier, S. A., Allegrini, F., Bzowski, M., et al. 2012, ApJ, 754, 14
Fuselier, S. A., Bochsler, P., Chornay, D., et al. 2009, SSRv, 146, 117
Galli, A., Fok, M.-C., Wurz, P., et al. 2008a, JGR, 113, E00B15
Galli, A., Wurz, P., Barabash, S., et al. 2006a, ApJ, 644, 1317
Galli, A., Wurz, P., Kallio, E., et al. 2008b, JGR, 113, E12012
Galli, A., Wurz, P., Lammer, H., et al. 2006b, SSRv, 126, 447
Grigoriev, A. 2007, PhD thesis, Swedish Institute of Space Physics, Kiruna
Gruntman, M., Roelof, E. C., Mitchell, D. G., et al. 2001, JGR, 106, 15767
Hilchenbach, M., Hsieh, K. C., Hovestadt, D., et al. 1998, ApJ, 503, 916
Kallenbach, R., Hilchenbach, M., Chalov, S. V., Le Roux, J. A., & Bamert, K. 2005, A&A, 439, 1
Krimigis, S. M., Mitchell, D. G., Roelof, E. C., Hsieh, K. C., & McComas, D. J. 2009, Sci, 326, 971
Marsch, E., Mühlhäuser, K.-H., Schwenn, R., et al. 1982, JGR, 87, 52
Martinecz, C., Fränz, M., Woch, J., et al. 2008, P&SS, 56, 780
McComas, D. J., Allegrini, F., Bochsler, P., et al. 2009a, SSRv, 146, 11
McComas, D. J., Allegrini, F., Bochsler, P., et al. 2009b, Sci, 326, 959
McComas, D. J., Bzowski, M., Frisch, P., et al. 2010, JGR, 115, A09113
McComas, D. J., Dayeh, M. A., Allegrini, F., et al. 2012, ApJS, 203, 1
Reisenfeld, D. B., Allegrini, F., Bzowski, M., et al. 2012, ApJ, 747, 110
Richardson, J. D., Kasper, J. C., Wang, C., Belcher, J. W., & Lazarus, A. J. 2008, Natur, 454, 63
Schläppi, B., Altwegg, K., Balsiger, H., et al. 2010, JGR, 115, A12313
Schwadron, N. A., Allegrini, F., Bzowski, M., et al. 2011, ApJ, 731, 56
Sokół, J. M., Bzowski, M., Tokumaru, M., Fujiki, K., & McComas, D. J. 2013, SoPh, 285, 167
Wieser, M., Wurz, P., Möbius, E., et al. 2007, RScI, 78, 124502
Wood, B. E., Izmodenov, V. V., Linsky, J. L., & Malama, Y. G. 2007, ApJ, 657, 609
Wurz, P., Fuselier, S. A., Möbius, E., et al. 2009, SSRv, 146, 173
Wurz, P., Galli, A., Barabash, S., & Grigoriev, A. 2008, ApJ, 638, 248
Zank, G. P., Heerikhuisen, J., Pogorelov, N. V., Burrows, R., & McComas, D. J. 2010, ApJ, 708, 1092